

Supporting Information

Zero-dimensional nickel, iron-metal-organic framework (MOF) for synergistic N₂ electrofixation

Jingjing Duan,^a Yuntong Sun,^b Sheng Chen,^{*a,b} Xianjue Chen,^a and Chuan Zhao^{*a}

^a School of Chemistry, The University of New South Wales, Sydney, New South Wales 2052, Australia

^b Key Laboratory for Soft Chemistry and Functional Materials, Nanjing University of Science and Technology, Ministry of Education, Nanjing, 210094, China

E-mail: sheng.chen@njust.edu.cn; chuan.zhao@unsw.edu.au

I. Experimental Section

1. Material Synthesis

Chemicals. Nickel acetate ($\text{Ni}(\text{Ac})_2 \cdot 4\text{H}_2\text{O}$, 98%), iron chloride ($\text{FeCl}_3 \cdot 6\text{H}_2\text{O}$, 98%), copper(II) acetate ($\text{Cu}(\text{Ac})_2$, 98%), 2,6-Naphthalenedicarboxylic acid dipotassium ($\text{C}_{10}\text{H}_6(\text{CO}_2\text{K})_2$, 95%), active carbon (98%), sodium bicarbonate (NaHCO_3 , 99%), Nafion membrane, sodium hydroxide (NaOH , 99%), salicylic acid ($\text{C}_7\text{H}_6\text{O}_3$, 98%), sodium citrate ($\text{Na}_3\text{C}_6\text{H}_5\text{O}_7$, 99%), sodium hypochlorite (NaClO , 99%), sodium nitroferricyanide ($\text{C}_5\text{FeN}_6\text{Na}_2\text{O}$, 99.5%), para-(dimethylamino) benzaldehyde ($\text{C}_9\text{H}_{11}\text{NO}$, 99%), ethanol (100%), and ammonia assay kit, ammonia standard solution (5%), hydrazine (85%), $^{15}\text{N}_2$ labeling gas, ($^{14}\text{NH}_4$) $_2\text{SO}_4$, ($^{15}\text{NH}_4$) $_2\text{SO}_4$ were purchased from Sigma-Aldrich and directly used without further treatment or purification. All aqueous solutions were prepared with high-purity de-ionized water (DI-water, resistance 18 $\text{M}\Omega \text{ cm}^{-1}$).

Synthesis of bulk NiFe-MOF. 1 mL of DI-water was mixed with 8 mg of $\text{Ni}(\text{Ac})_2 \cdot 4\text{H}_2\text{O}$ and 2 mg of $\text{FeCl}_3 \cdot 6\text{H}_2\text{O}$. Next, 10 mg of organic ligand (2,6-naphthalenedicarboxylate tetrahydrate) was added into the above solution, and the vial was sealed for reaction at 60 °C for 20 hrs. After cooling down to room temperature, the product was collected by centrifugation, and washed with copious water for several times.

Synthesis of NiFe-MOF. The bulk NiFe-MOF material (300 mg) was dispersed in DI-water in a mortar with initial concentration of 100 mg mL^{-1} . After grinding for 10 min, the dispersion was transferred to a glass vial containing 30 ml DI-water, followed by sonication for 6 hrs at the power of 200 W in an ice-bath. After that, the suspension was collected by centrifugation at 1000 rpm for 10 mins. According to XPS in Figure 2c-d in the main text, the mass percentatge of Fe is 3.1 wt% inside the material.

Synthesis of Ni-MOF. The preparation procedure is similar to NiFe-MOF counterpart by using only 10 mg of $\text{Ni}(\text{Ac})_2 \cdot 4\text{H}_2\text{O}$ as metal precursor. The mass percentatge of Fe is 0 wt% inside the material.

Synthesis of Fe-MOF. The preparation procedure is similar to NiFe-MOF counterpart by using only 10 mg of $\text{FeCl}_3 \cdot 6\text{H}_2\text{O}$ as metal precursor. The mass percentage of Fe is 15.5 wt% inside the material.

Synthesis of NiFe-MOF doped with 7.7 wt% Fe. The sample has been synthesized similarly to the NiFe-MOF except by tuning the mass of metal salts as 5 mg of $\text{Ni}(\text{Ac})_2 \cdot 4\text{H}_2\text{O}$ and 5 mg of $\text{FeCl}_3 \cdot 6\text{H}_2\text{O}$.

Synthesis of CuFe-MOF. The preparation procedures are similar to NiFe-MOF counterparts by replacing nickel salt with 8 mg of copper acetate.

Synthesis of CoFe-MOF. The preparation procedure is similar to NiFe-MOF counterpart by replacing nickel salt with 8 mg of cobalt acetate.

Synthesis of MnFe-MOF. The preparation procedure is similar to NiFe-MOF counterpart by replacing nickel salt with 8 mg of manganese acetate.

2. Physical Characterization

XRD was performed on a Philips 1130 X-ray diffractometer (40 kV, 25 mA, Cu $K\alpha$ radiation, $\lambda=1.5418 \text{ \AA}$); XPS was performed on an Axis Ultra (KratosAnalytical, UK) XPS spectrometer equipped with an Al $K\alpha$ source (1486.6 eV); AFM was conducted on Bruker Dimension ICON SPM using peak force mode; morphologies of the samples were observed on TEM (JEOL JEM-ARM200F) and SEM (QUANTA 450); UV-vis spectra were performed on a SHIMADZU UV-2600 spectrophotometer; zeta potential was recorded on a Malvern Zetasizer Nano series analyser; XANES measurements were carried out at the SAXS/WAXS beamline of the Australian Synchrotron; inductively coupled plasma optical emission spectrometer (ICP-OES) was conducted on a Thermo Scientific iCAP 6500 duo optical emission spectrometer fitted with a simultaneous charge induction detector; Fourier transform infrared spectra (FTIR) were recorded on a Nicolet 6700 spectrometer; further, the porosity was evaluated by using nitrogen adsorption-desorption isotherms measured at 77 K on a TriStar II 3020 Micrometrics apparatus.

3. Electrochemical Characterizations

Electrochemical setup. The electrochemical testing was carried out on a CHI760 workstation using H-type electrolytic configuration with MOF working electrode, platinum foil counter electrode, Ag/AgCl reference electrode, Nafion membrane, and 0.1 M NaHCO₃ electrolyte. Note that nafion may come contaminated and can absorb and release ammonia. Therefore, the Nafion membrane was pre-treated in H₂O₂ (5%) aqueous solution and DI-water at 80 °C for 1 hr, respectively. Further, NaHCO₃ has been used as the electrolyte because of its low cost, earth abundance, high solubility to N₂ feedstock. All reported potentials were converted to RHE according to the Nernst equation:¹ $E_{\text{RHE}} = E_{\text{Ag/AgCl}} + 0.059 \text{ pH} + 0.205$, and all current densities was normalized to the geometric surface area.

Working electrode preparation. 1 mg of NiFe-MOF, 0.2 mg of carbon black, 5 μL of Nafion solution (5 wt%) were dispersed in 100 μL of isoproponal by ultrasonication for 1 hr to form a homogeneous ink. Then, the dispersion was loaded onto a glassy carbon substrate with area of 0.5 cm² and loading level of 1 mg cm⁻² or 3 mg cm⁻² followed by dry under ambient conditions.

Electrochemical NRR testing. Linear sweep voltammogram (LSVs) and cyclic voltammogram (CVs) plots were performed at the scan rates from 5-25 mV s⁻¹. Differential pulse voltammetry analysis was conducted with a pulse width of 0.2 s, pulse period of 0.5 s, amplitude of 50 mV, increased potential of 4 mV and sample width of 0.0167 s. Before data collection, the working electrodes were scanned several times until stabilization was reached in the whole system. NRR was tested in N₂ saturated 0.1 M NaHCO₃ solutions by purging the electrolyte with N₂ for 30 min before the measurement. For comparison, electrochemical tests in Ar-saturated solution were also conducted in this work.

Determination of ammonia by indophenol blue method. Ammonia concentration was firstly determined by the indophenol blue method using UV-vis spectra.^{1, 2} In detail, 2 mL aliquot of electrolyte was taken from the electrochemical cell, which was then mixed with 2

mL of a 1 M NaOH solution containing 5 wt% salicylic acid and 5 wt% sodium citrate, 1 mL of 0.05 M NaClO, and 0.2 mL of an aqueous solution of 1 wt % $C_5FeN_6Na_2O$ (sodium nitroferricyanide). After 2 hr under ambient conditions, the UV-vis absorption spectrum was measured, and the as-formed indophenol blue was determined at the absorption peak of 655 nm. The amount of ammonia is then determined by comparing the UV-vis peak at 340 nm at Ar and N_2 atmosphere.

Determination of ammonia by ammonia assay kit. To further verify the ammonia production from NRR, the ammonia concentration was also determined by the ammonia assay kit method using UV-vis spectra. The principle is presented in the inset of Fig. S11, and takes advantage of L-glutamate dehydrogenase for reacting with ammonia. The amount of ammonia is then determined by comparing the UV-vis peak at 340 nm at 0 and 5 mins.

$^{15}N_2$ isotope labelling experiment. An isotopic labelling experiment with $^{15}N_2$ enriched feeding gas can clarify the source of ammonia. During the labelling experiment, an acid trap was used to remove possible impurities from the gas supply. A low-velocity gas flow system (approximately 5 mL min^{-1}) was adopted due to the limited supply and price of $^{15}N_2$ gas. After NRR for 6 h, the obtained $^{15}NH_4^+$ was identified using 1H (nuclear magnetic resonance, 400 MHz) NMR spectroscopy with the data corrected by water peak.

Determination of hydrazine. The as-produced hydrazine was estimated by the method of Watt and Chrisp.^{1,2} Typically, a mixture solution of para-(dimethylamino) benzaldehyde (3 g), DI-water (15 mL) and ethanol (15 mL) was used as a colour reagent. 5 mL of above prepared colour reagent was mixed with 5 mL of electrolyte, and stirring 10 mins at room temperature; The UV-vis absorbance of the resulting mixed solution was measured at 455 nm.

Faradaic efficiency calculation. Faradaic efficiency (FE%) is defined as the quantity of charge consumed for synthesizing ammonia divided the total electric charge passed through the electrodes during the NRR. The total amount of ammonia was determined by using methods mentioned above. If we assume three electrons are required for producing one NH_3

molecule, the Faradaic efficiency is calculated as follows:

$$FE = 3F \times c(\text{NH}_3) \times V / (17 \times Q)$$

And the rate of ammonia formation was calculated using the following equation:

$$Y(\text{NH}_3) = c(\text{NH}_3) \times V / (t \times m)$$

where F is the Faraday constant, $c(\text{NH}_3)$ is ammonia concentration, V is the volume of electrolyte, t is the reaction time m is the catalyst mass, and Q is columbic charge.

Further, the corresponding energy efficiency (EE) is calculated according to the following formula on the basis of the equilibrium potential of NRR (E_{eq}), which is 0.581 V in neutral electrolyte (PH = 7):

$$EE = FE \times E_{eq} / (E_{eq} + \eta)$$

The turnover frequency (TOF) is calculated according to ammonia yield rate converting to molar mass of catalyst. As shown in the XPS spectra in Figures 2c-e, the chemical formula of NiFe-MOF is $\text{Ni}_{0.81}\text{Fe}_{0.19}(\text{C}_{12}\text{H}_6\text{O}_4)(\text{H}_2\text{O})_4$, which corresponds to the molar mass (M_{catalyst}) of 335.6 g mol⁻¹. If we assume metal sites (Ni and Fe) are active centers for NRR, then:

$$\begin{aligned} \text{TOF} &= n(\text{NH}_3) / n(\text{Catalyst active sites}) / t \\ &= [c(\text{NH}_3) \times V / M_{\text{NH}_3}] / [(0.81 + 0.19) \times m / M_{\text{catalyst}}] / t \\ &= [c(\text{NH}_3) \times V / (t \times m)] \times [M_{\text{catalyst}} / M_{\text{NH}_3}] \\ &= Y(\text{NH}_3) \times [M_{\text{catalyst}} / M_{\text{NH}_3}] \end{aligned}$$

4. Computational details

All spin-polarized density functional theory calculations under periodic boundary conditions were performed with Generalized Gradient Approximation method with Perdew-Burke-Ernzerhof (PBE)³ functionals for the exchange-correlation term using projector-augmented-wave (PAW)⁴ pseudopotentials implemented in Vienna Ab-initio Simulation Package (VASP).^{5, 6} Hubbard-U correction method (DFT+U) was carried out to improve the description of highly correlated Ni/Fe 3d orbitals with the value of U set to 4.0/6.4 eV. The

energy cutoff of 450 eV for plane-wave expansion was demonstrated sufficient to achieve the convergence of the calculated properties. The DFT-D3(BJ)⁷ method was used to describe the dispersion effects in the system. All the geometric structures of adsorption intermediates were optimized using a force-based conjugate gradient algorithm until the forces on all the relaxed atoms were below 0.05 eV/Å.

According to the XRD pattern in Figure 2b, one of the prominent peaks for NiFe-MOF is located at 8.63 degree, which corresponds to the layer spacing of 0.98 nm for two adjacent metal-oxygen-layers (MO₆ units; M = Ni or Fe). Accordingly, we define the structural model of NiFe-MOF in DFT calculation as follows: nickel ion is present in the form of [NiO₆] octahedral coordination; and two [NiO₆] units are coordinated to two trans monodentate carboxylates. Principally, Fe could replace either Ni center or oxygen atom inside [NiO₆] octahedra, which forms [FeO₆] octahedra or Ni-Fe bondings in the MOF structure. Therefore, we have carefully analyzed the XPS (Figures 2c-e) and XAS (Figures 4c,d), but have not seen the formation of Ni-Fe bondings. Consequently, we propose that Fe has *in situ* replaced Ni centers, which formed [FeO₆] octahedra just by [NiO₆] inside the MOF structure.

During the geometry optimization, the margin NiO₆ was fixed while others and adsorbates could be relaxed. Over these optimised geometries, vibrational frequencies were calculated in order to obtain zero-point energies (ZPE), thermal corrections and entropy contributions. In such cases, all Ni/Fe-MOF were frozen during vibrational frequency calculations, imposing no constrains for N and H atoms.

Gibbs free energy calculation has been carried out as it follows:

$$G = E + \int C_p dT - T_s$$

where G, E and C_p refer to the chemical potential (partial molar Gibbs free energy), electronic energy and heat capacity, respectively. The entropy term can be expressed as the sum of the translational, rotational, vibrational and electronic contributions as to:

$$S = S_t + S_r + S_v + S_e$$

Finally, intrinsic zero-point energy (ZPE) and extrinsic dispersion (D) corrections can be included to finally obtain:

$$G = E + \int C_p dT - T(S_t + S_r + S_v + S_e) + ZPE + D$$

Since $S_e \approx 0$ at the fundamental electronic level.

For the case of solids and adsorbates, some approximations can be assumed:

- (i) As for gases, at the fundamental electronic level $S_e \approx 0$.
- (ii) Translational and rotational motions can be neglected, therefore, $S_t \approx 0$ and $S_r \approx 0$. In this sense, all entropy contributions comes from vibrations: $S = S_v$. Similarly, translational and rotational contributions to the heat capacity are neglected.

Therefore, Gibbs free energies for the different states have been calculated as to:

$$G = E + \int C_p dT - TS_v + ZPE + D$$

II. Supplementary Results

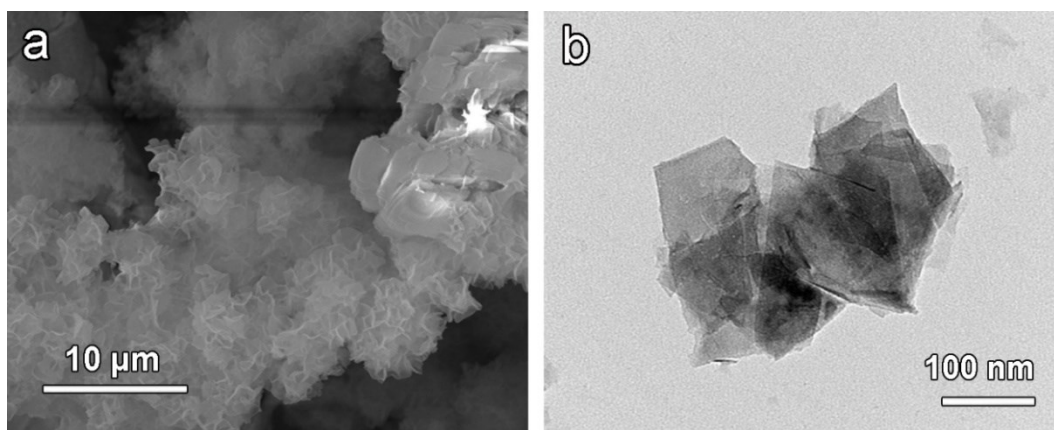
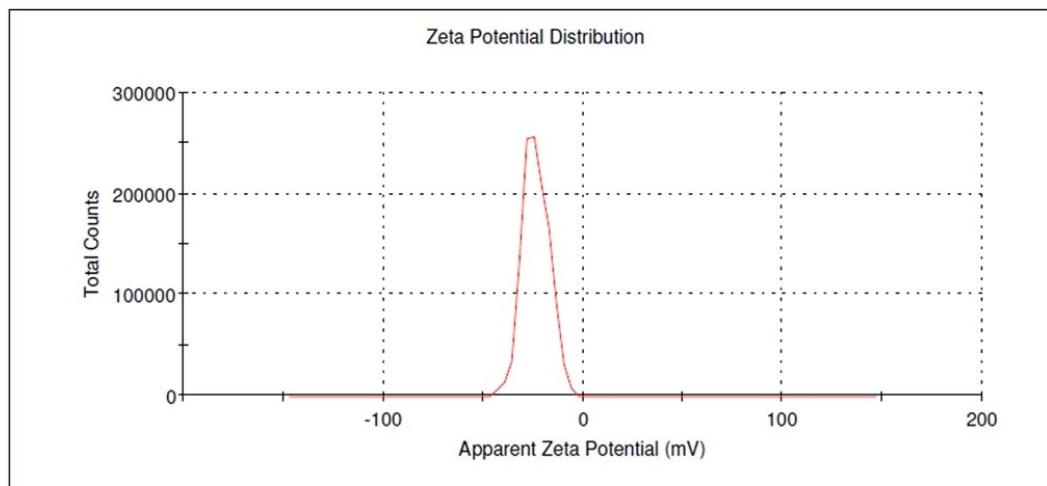


Figure S1: SEM and TEM images of bulk MOF, showing the particle size ranging from several hundred nanometres to a few micrometers. It should be noted that SEM can only observe the morphology of dried samples. Thus NiFe-MOF has been freeze-dried to form powders for SEM testing. During this process, nanosheets become aggregated owing to the interlayer *van deer waals* forces.

a

	Mean (mV)	Area (%)	St Dev (mV)
Zeta Potential (mV): -23.6	Peak 1: -23.6	100.0	6.63
Zeta Deviation (mV): 6.63	Peak 2: 0.00	0.0	0.00
Conductivity (mS/cm): 0.0316	Peak 3: 0.00	0.0	0.00

Result quality **Good**



b

	Mean (mV)	Area (%)	St Dev (mV)
Zeta Potential (mV): -10.0	Peak 1: -10.0	100.0	3.45
Zeta Deviation (mV): 3.45	Peak 2: 0.00	0.0	0.00
Conductivity (mS/cm): 0.144	Peak 3: 0.00	0.0	0.00

Result quality **Good**

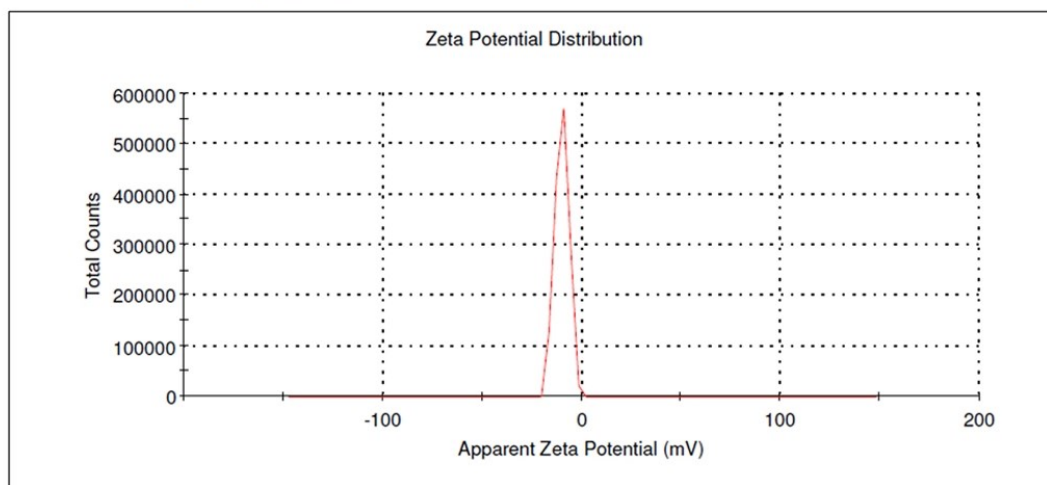


Figure S2: Zeta potential analysis of (a) NiFe-MOF and (b) bulk MOF.

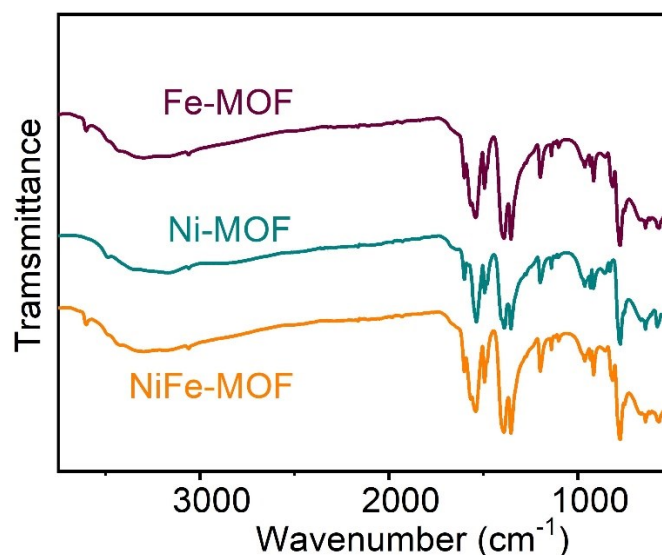


Figure S3: FT-IR spectra of NiFe-MOF, Ni-MOF, and Fe-MOF.

Supplementary note.

We have done a number of physical characterizations for NiFe-MOF and their mono-metal counterparts. Firstly, the apparent color for NiFe-MOF is brownish yellow, which is similar to Fe-MOF and different from individual Ni-MOF (light blue). Secondly, the mass densities of these three MOF samples are almost the same, which are in the range of 0.485~0.50 g cm⁻³. Further, we have conducted additional FT-IR analyses for Fe-MOF, Ni-MOF, and NiFe-MOF. As shown in above Figure S3, all these spectra show similar characteristic peaks in the range from 1000-2000 cm⁻¹ that originated from organic ligand from MOF structures.

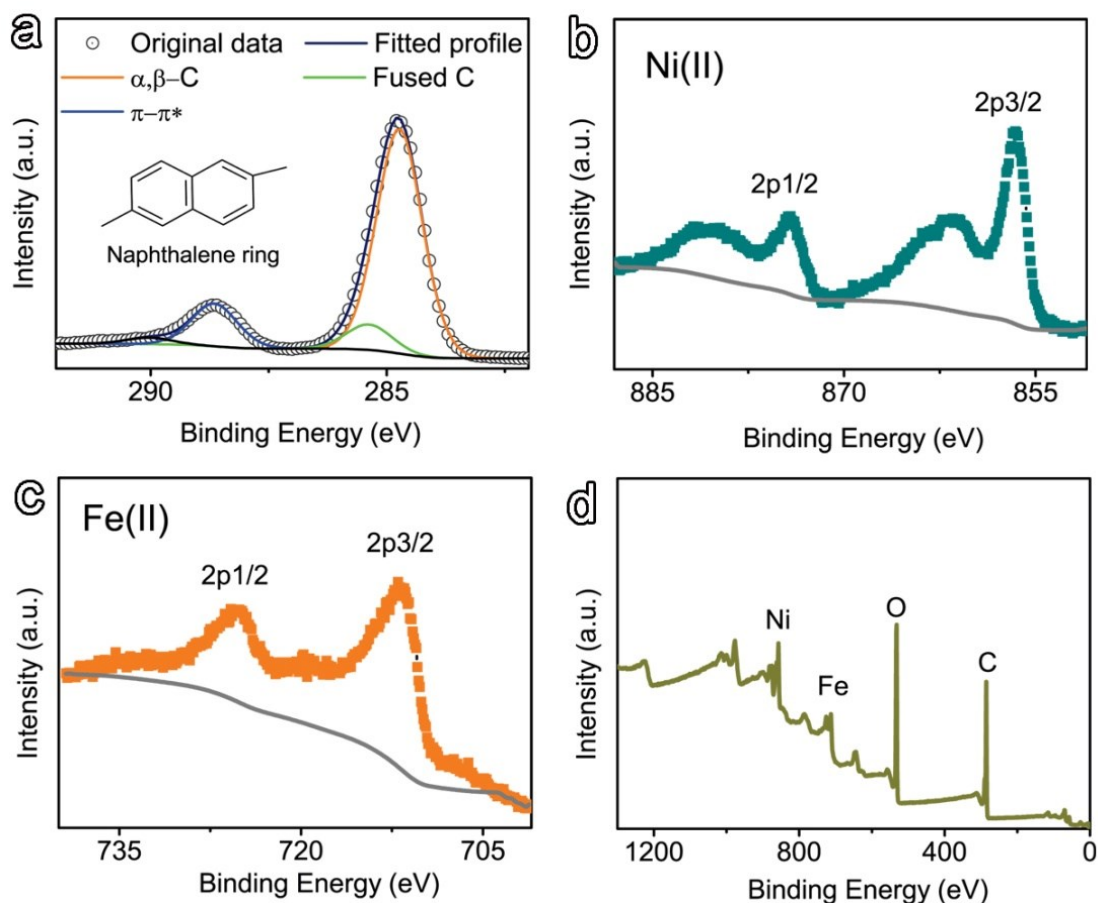


Figure S4: XPS spectra of bulk MOF: (a) C1s, (b) Ni2P, (c) Fe2p, (d) overall survey.

Supplementary note.

Our MOF material consists of alternating organic hydrocarbon (2,6-naphthalenedicarboxylic group) coordinated with inorganic $[\text{NiO}_6]$ octahedra. Therefore, Fe could replace either nickel (Ni) center or oxygen atom inside $[\text{NiO}_6]$ octahedra, which forms either $[\text{FeO}_6]$ octahedra or Ni-Fe bondings in the MOF structure. Consequently, we have carefully analyzed the XPS (Figures 2c-e) and XAS (Figures 4c,d), but have not seen the formation of Ni-Fe bondings. Therefore, we propose that Fe has in situ replaced Ni centers, which formed $[\text{FeO}_6]$ octahedra just by $[\text{NiO}_6]$ inside the MOF structure. This phenomenon is similar to that of many reports in the literature, such as amorphous nickel-iron system⁸ and single-stom Au/NiFe layered double hydroxide.⁹

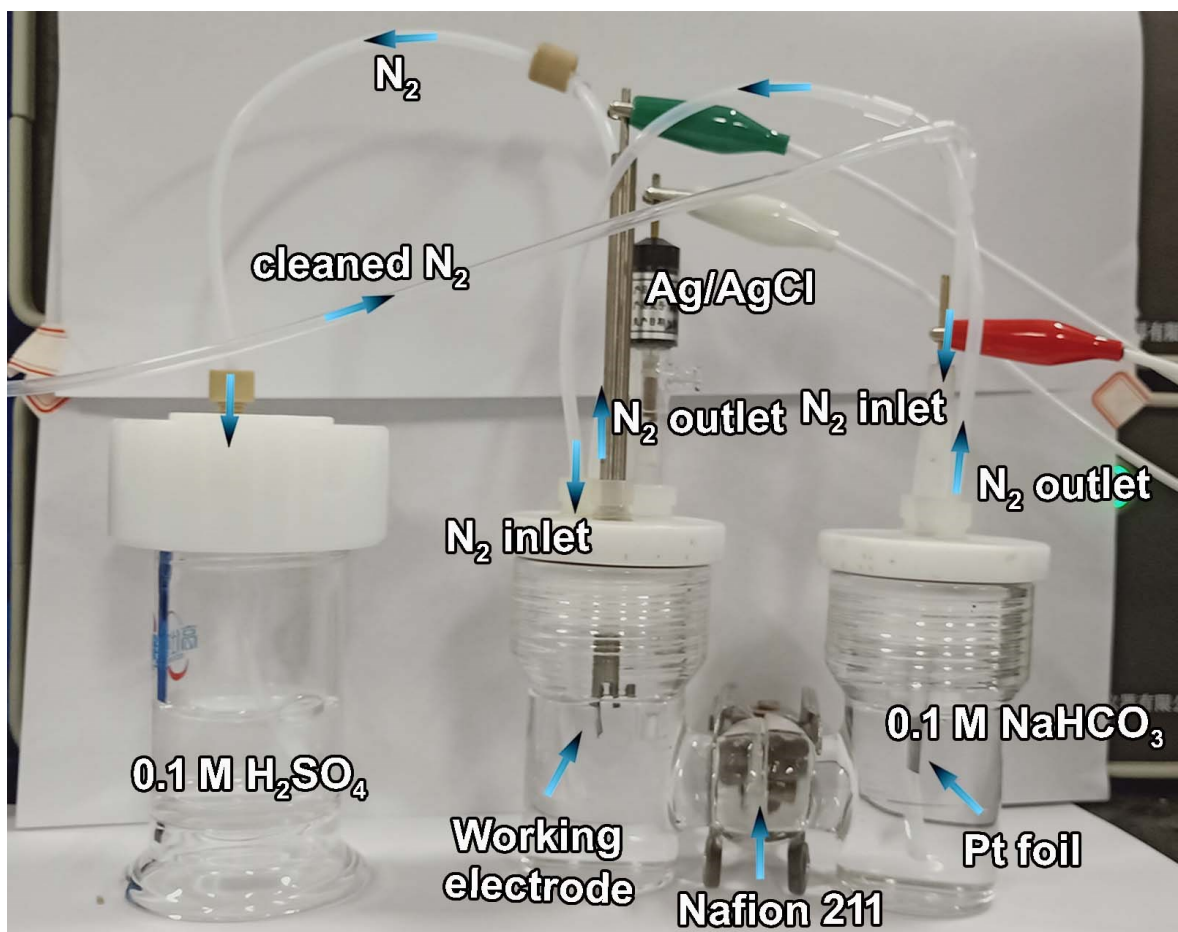


Figure S5: A digital photograph of electrochemical H-type cell, which contains of the following components: i) working electrode prepared by depositing MOF catalyst on glassy carbon with a mass loading of 1 mg cm^{-2} ; ii) counter electrode composed of platinum foil ($3 \text{ cm} \times 1 \text{ cm} \times 0.1 \text{ mm}$); iii) reference electrode composed of Ag/AgCl electrode; iv) separation membrane composed of Nafion 211; v) 35 mL aqueous electrolyte composed of 0.1 M NaHCO_3 ; vi) gas tubes for N_2 gas in and out; vii) exhaustive gas tube composed of 0.1 M H_2SO_4 .

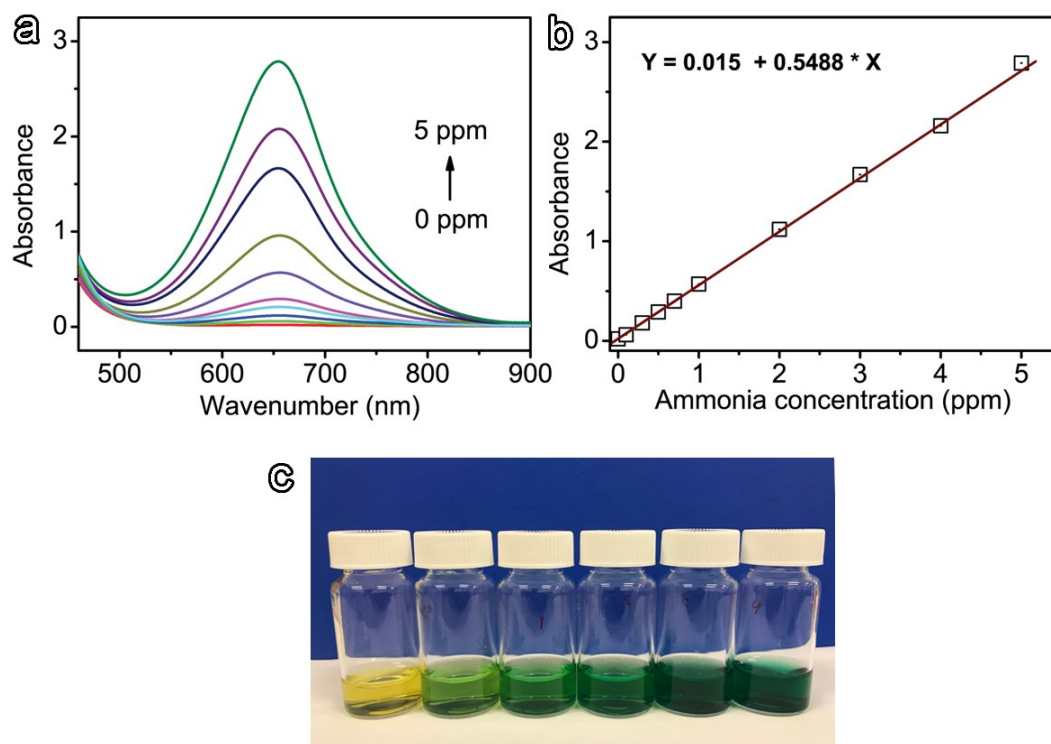


Figure S6: Absolute calibration of the indophenol blue method using ammonium solutions of known concentration as standards. (a) UV-Vis curves of indophenol assays with ammonium after incubated for 2 hours at room temperature; (b) calibration curve used for ammonium concentration. The absorbance at 655 nm was measured by UV-Vis spectrophotometer, and the fitting curve shows good linear relation of absorbance with ammonium concentration ($y = 0.0154 + 0.05488X$) of three times independent calibration curves. (c) shows the optical image of indophenol indicator with ammonia concentrations from 0, 0.5, 1, 2, 3, 4 ppm from left to right.

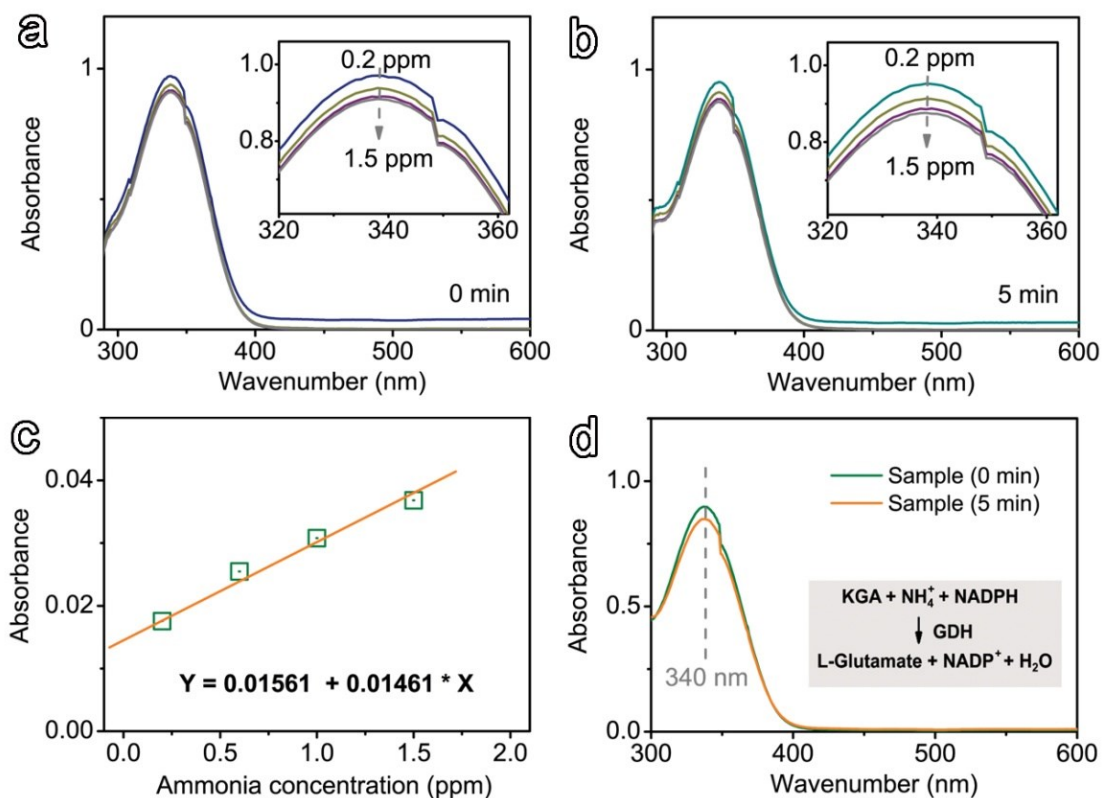


Figure S7: Absolute calibration of the ammonia assay kit method for estimating ammonia concentration, using ammonia solutions of known concentration as standards. (a,b) UV-Vis curves of various ammonia concentration after incubated for 0 and 5 mins at room temperature; (c) calibration curve used for estimation of ammonia concentration. The absorbance at 340 nm was measured by UV-Vis spectrophotometer, and the fitting curve shows good linear relation of absorbance with ammonia concentration ($y = 0.01561 + 0.01462X$) of three times independent calibration curves; (d) UV-Vis curves of ammonia assay kit method with NiFe-MOF electrocatalyst after reaction at -347 mV (vs. RHE) for 20 hrs in nitrogen atmosphere.

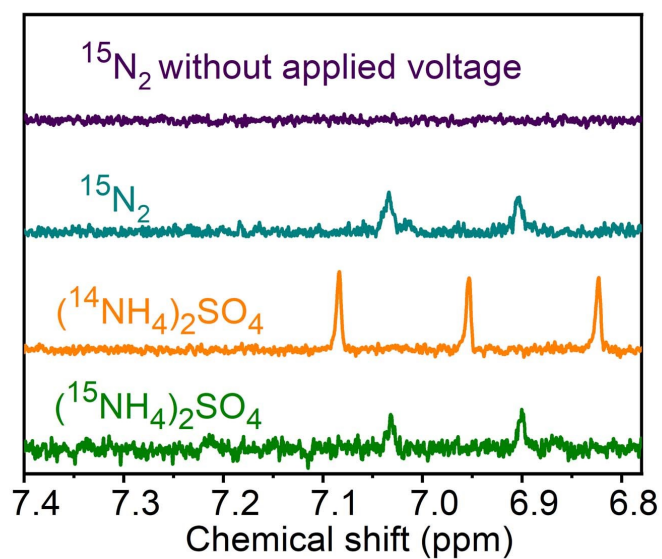


Figure S8: ^1H NMR spectra (400 MHz) shows $^{15}\text{NH}_4^+$ produced from the NRR reaction using $^{15}\text{N}_2$ as the isotopic N_2 source. Consequently, the Faradaic efficiency for NiFe-MOF is calculated as 10.9%, and ammonia yield is $9.0 \mu\text{g h}^{-1} \text{mg}^{-1}_{\text{cat}}$, both of which are comparable to the results determined by using $^{14}\text{N}_2$ as the feeding gas from other methods.

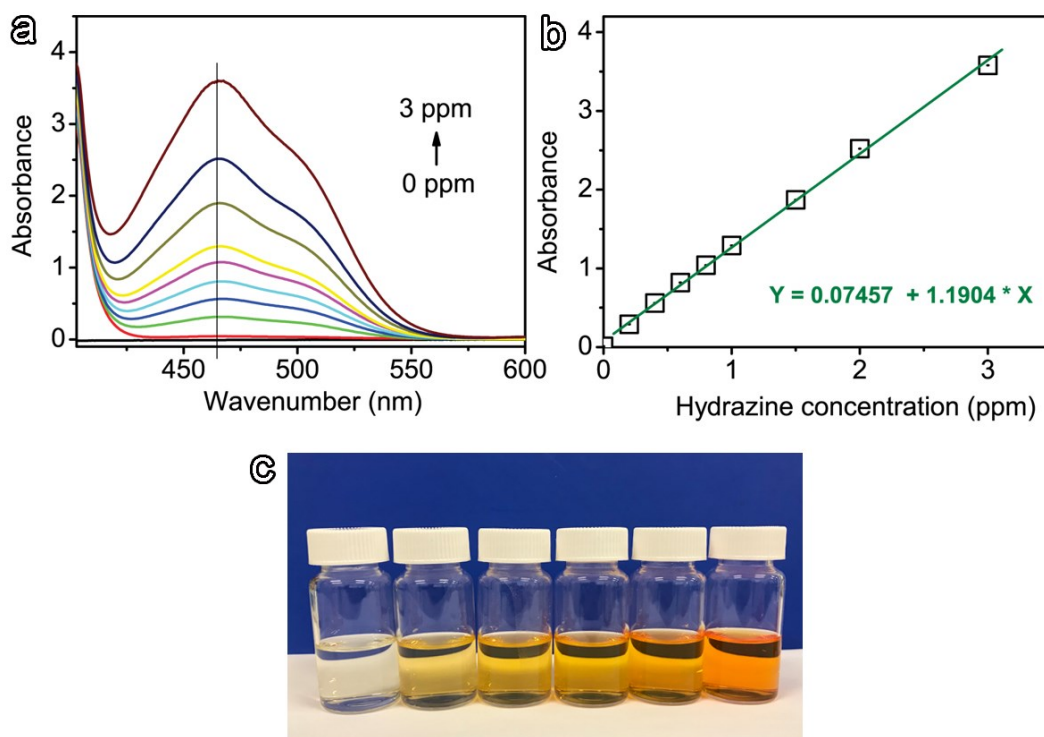


Figure S9: Absolute calibration of the Watt and Chrisp (para-dimethylamino-benzaldehyde) method for estimating $N_2H_4 \cdot H_2O$ concentration, using $N_2H_4 \cdot H_2O$ solutions of known concentration as standards. (a) UV-Vis curves of various $N_2H_4 \cdot H_2O$ concentration after incubated for 10 min at room temperature; (b) calibration curve used for estimation of $N_2H_4 \cdot H_2O$ concentration. The absorbance at 455 nm was measured by UV-Vis spectrophotometer, and the fitting curve shows good linear relation of absorbance with $N_2H_4 \cdot H_2O$ concentration ($y = 0.07457 + 1.1904x$) of three times independent calibration curves; (c) shows the optical images of para-dimethylamino-benzaldehyde indicator with $N_2H_4 \cdot H_2O$ concentrations ranging from 0, 0.2, 0.4, 0.6, 0.8, 1 ppm (from left to right).

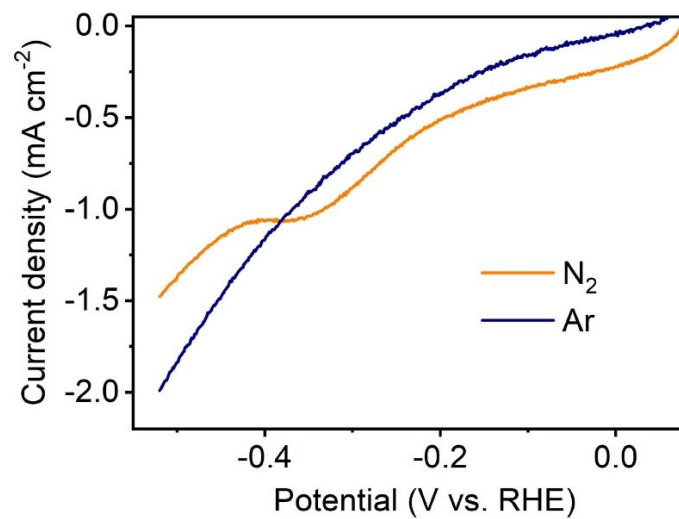


Figure S10: LSV plots for NiFe-MOF with a high catalyst loading of 3 mg cm⁻² in N₂ and Ar atmospheres, showing an obvious N₂ reduction peak at -347 mV (vs. RHE)

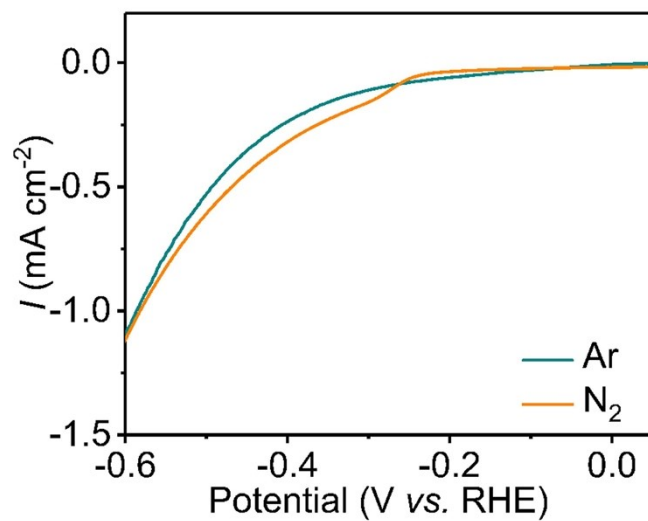


Figure S11: LSV plots for bulk NiFe-MOF with a catalyst loading of 1 mg cm⁻² in N₂ and Ar atmospheres, showing an obvious N₂ reduction peak at around -300 mV (vs. RHE).

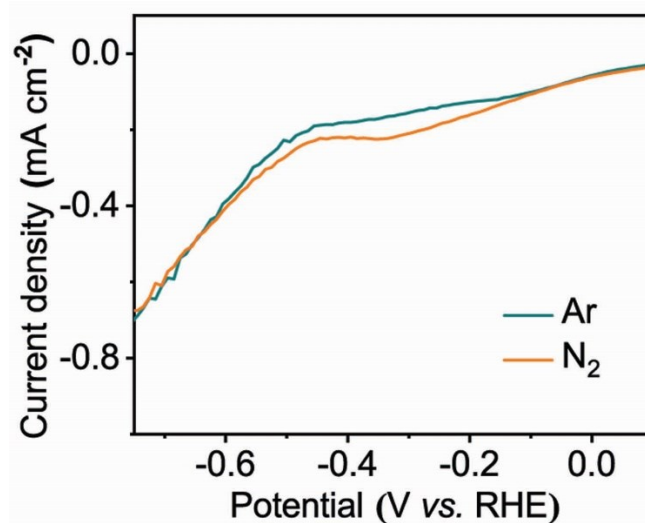


Figure S12: Differential pulse voltammetry analyses for NiFe-MOF in N₂ and Ar atmospheres, showing an obvious nitrogen reduction peak around -340 mV (vs. RHE).

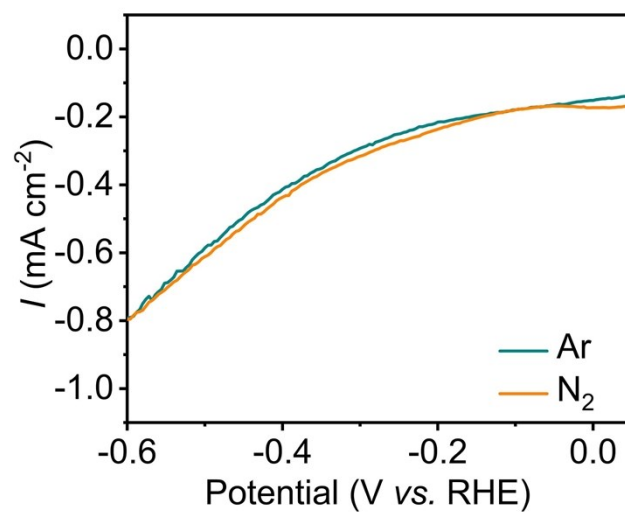


Figure S13: Differential pulse voltammetry analyses for bulk NiFe-MOF in N₂ and Ar atmospheres, where the obvious current change in the range from -150 to 350 mV (vs. RHE) indicates the occurrence of nitrogen reduction reaction.

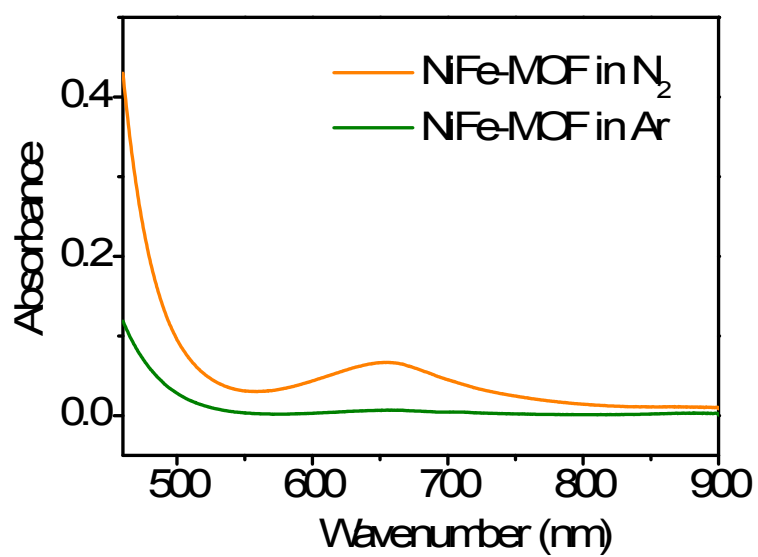


Figure S14: UV-Vis curves of indophenol assays with NiFe-MOF electrocatalyst after reaction at -347 mV (vs. RHE) for 1 hr in nitrogen and argon atmospheres

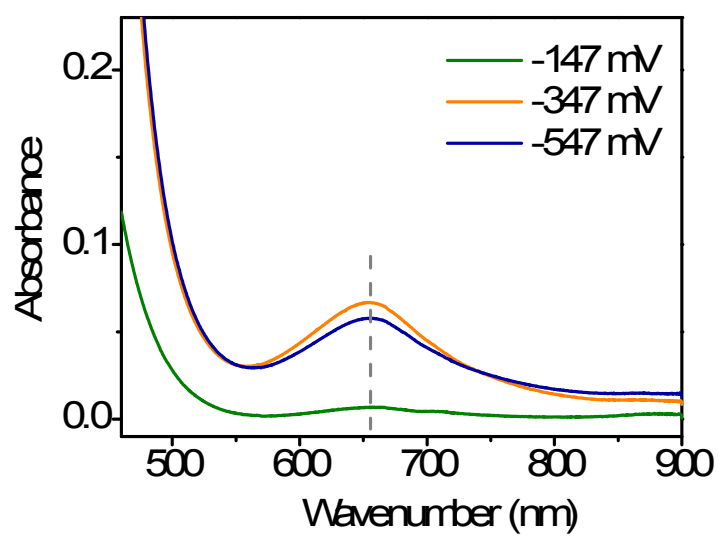


Figure S15: UV-Vis curves of indophenol assays with NiFe-MOF electrocatalyst after reaction at different potentials (vs. RHE) for 1 hour in nitrogen atmosphere.

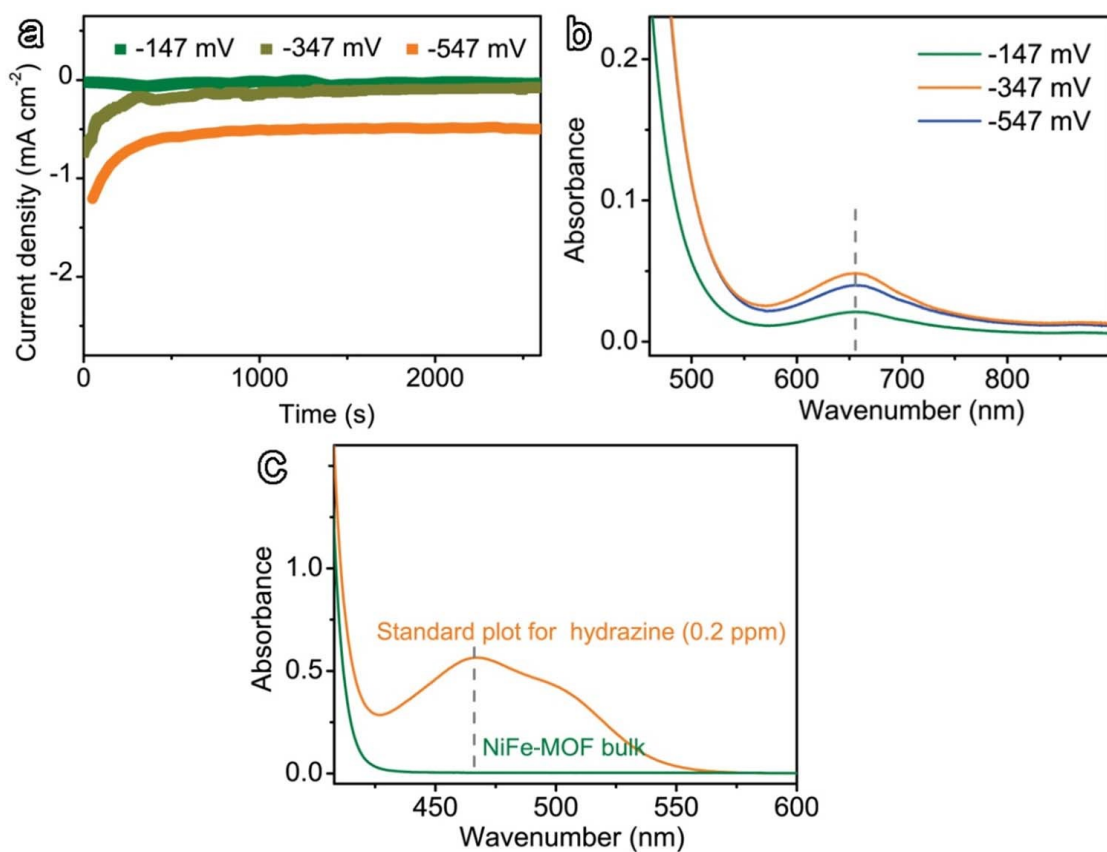


Figure S16: (a) Chronoamperometric response of bulk NiFe-MOF at different potentials (*vs.* RHE) in nitrogen atmosphere; (b) UV-Vis curves of indophenol assays with bulk NiFe-MOF MOF electrocatalyst after reaction at different potentials (*vs.* RHE) in nitrogen atmosphere; (c) UV-Vis curves of Watt and Chrisp assays with bulk MOF electrocatalyst after reaction at -347 mV (*vs.* RHE) for 1 hour in nitrogen atmosphere.

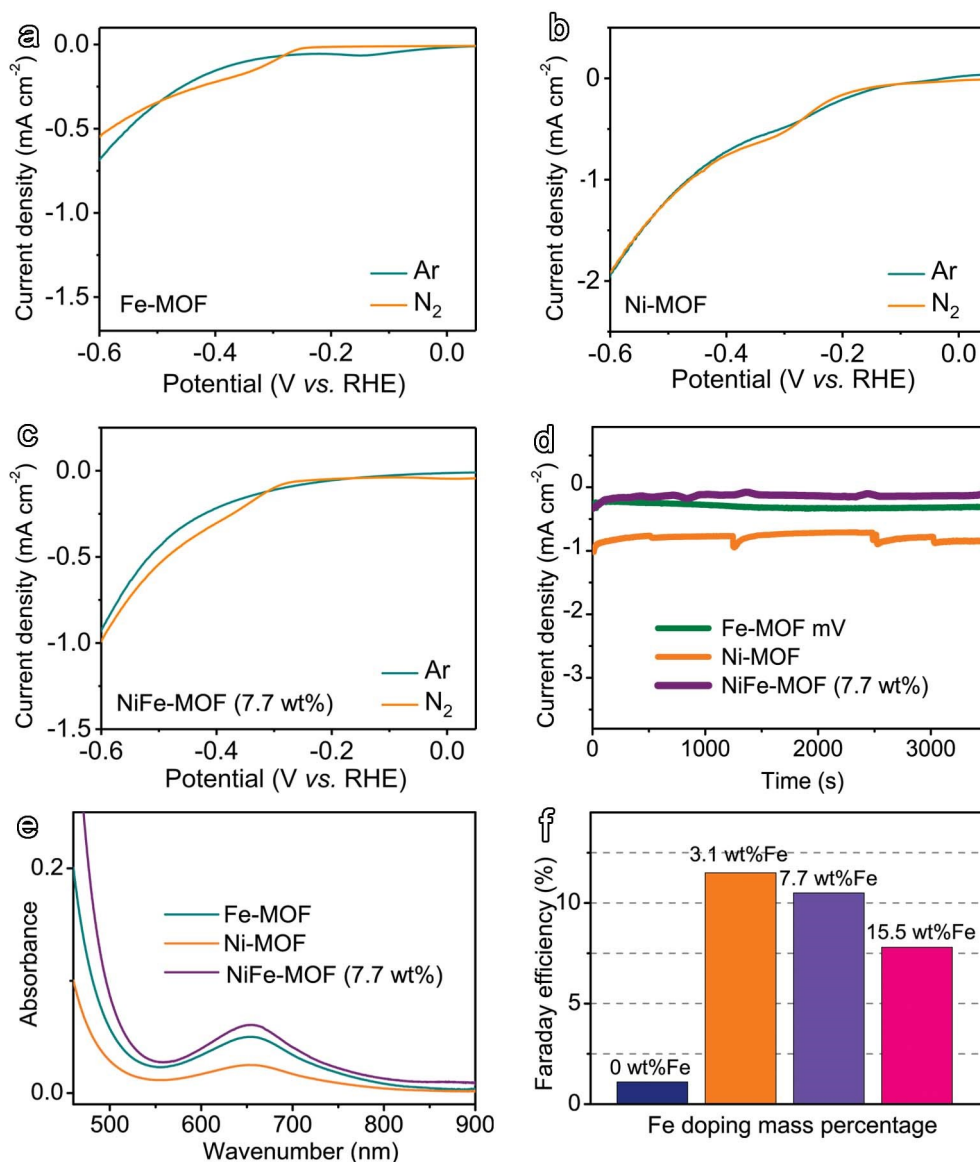


Figure S17: (a) LSV plots for Ni-MOF (0% Fe doping), NiFe-MOF (3.1% Fe doping), NiFe-MOF (7.7% Fe doping), and Fe-MOF (15.5% Fe doping) with a catalyst loading of 1 mg cm⁻² in N₂ and Ar atmospheres, showing an obvious N₂ reduction peak at -347 mV (vs. RHE); (b) chronoamperometric response of Ni-MOF, Fe-MOF, and NiFe-MOF (Fe-doping ratio of 7.7 wt%) at -347 mV (vs. RHE) in nitrogen atmosphere; (c) UV-Vis curves of indophenol assays for corresponding electrocatalysts; (d) Faraday efficiencies for corresponding electrocatalysts.

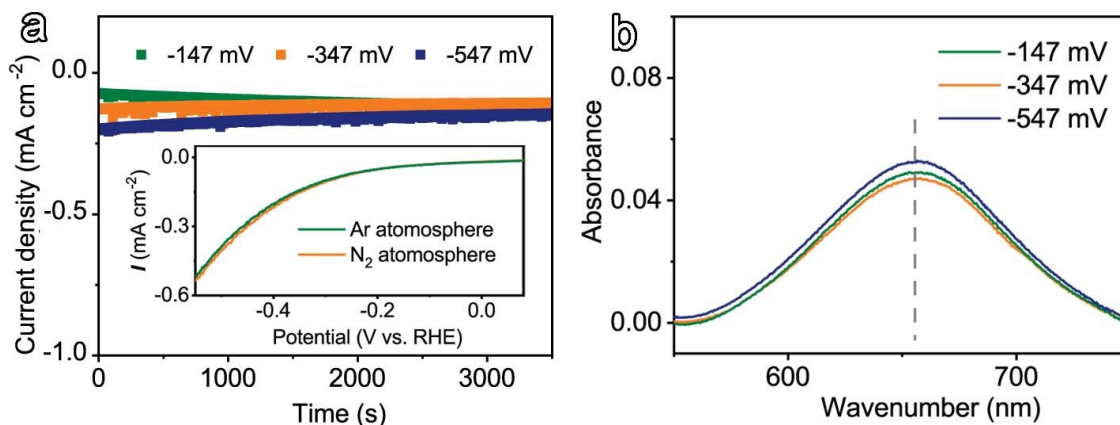


Figure S18: Electrocatalytic properties of NiFe metallic nanoparticles for nitrogen reduction reaction (NRR) under ambient conditions. (a) Chronoamperometric response at different potentials (vs. RHE); inset of (a) shows the LSV plots in nitrogen and argon atmospheres. (b) UV-vis curves of indophenol blue assays for ammonia detection. Note that the NiFe metallic nanoparticles have been prepared according to the literatures,¹⁰ which shows the Faradaic efficiency of 9.8%, 10.6% and 10.2%, and ammonia yield rate of 3.4, 5.8, 8.5 $\mu\text{g h}^{-1} \text{mg}^{-1}_{\text{cat}}$ at the potentials of -147 mV, -347 mV, and -547 mV (vs. RHE).

Supporting note.

There are three different characteristics that have contributed to better NRR performances as comparison to metallic NiFe nanoparticles:

Firstly, 0D NiFe-MOF is structurally metal-organic framework made of metal (Ni, Fe) site isolation coordinated with organic ligands (2,6-naphthalenedicarboxylate). Particularly, these metal active sites have molecular distribution that similar to traditional molecular catalysts. This structure feature can provide enormous active sites for promoting NRR process. In contrast, NiFe nanoparticles belong to heterogeneous catalysts that can only make use of the atoms on the outer surfaces, which exhibit relatively smaller available active centres for catalytic reactions.

Moreover, different from metallic NiFe nanoparticles, there are numerous micropores (0.7 and 1.7 nm) inside NiFe-MOF, as shown by the N_2 isotherm test (Figure S24). Traditionally, these micropores are deeply imbedded inside bulk MOF that cannot contribute to electrochemical process. In this work, we propose a downsizing strategy to make 0D NiFe-MOF; therefore, these pores can be effectively utilized for exposing more active sites and providing additional ion transport channels, which help improve NRR activities.

Further, metallic nanoparticles are known to be highly active for hydrogen evolution reaction (HER),¹¹ which is a completing side process for NRR. Generally, HER could consume the electrons otherwise used for NRR, therefore decrease the Faradic efficiency and ammonia yield rate for overall reaction. In contrast, HER efficiency can be effectively inhibited in 0D NiFe-MOF composed of metal-O bondings inside the structure (Please see FTIR in Figure S3). Therefore, NiFe-MOF can exhibit better activities toward NRR than NiFe nanoparticles.

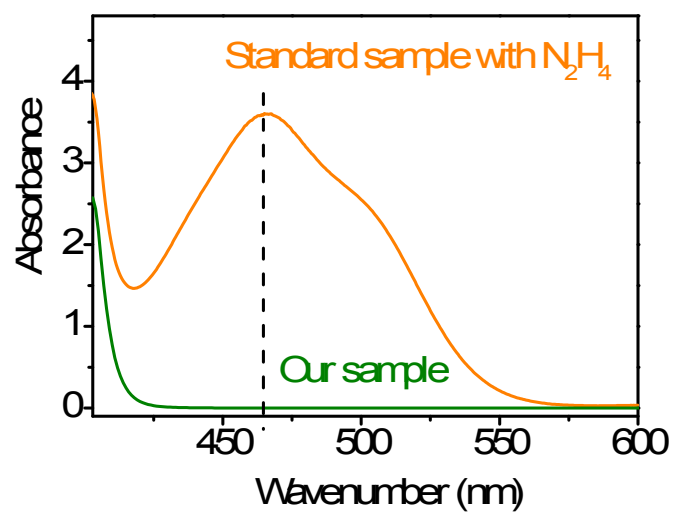


Figure S19: UV-Vis curves of Watt and Chrisp assays with NiFe-MOF electrocatalyst after reaction at -347 mV for 20 hrs in nitrogen atmosphere.

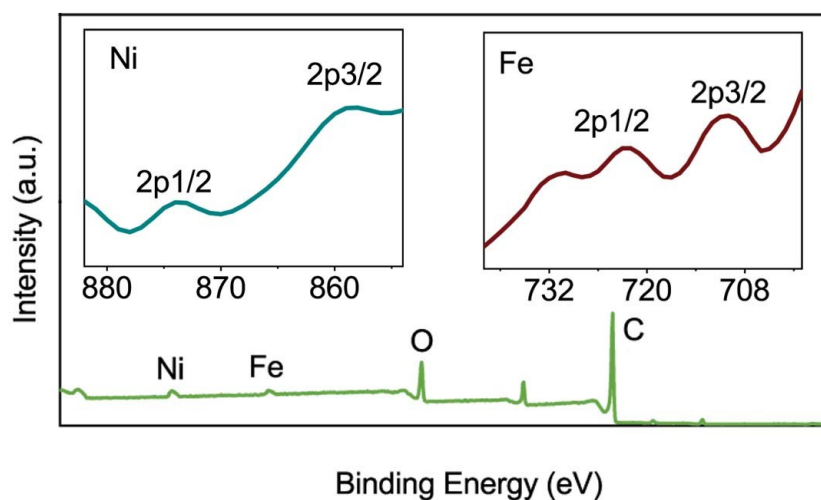


Figure S20: XPS characterizations of NiFe-MOF-based working electrode after reaction at -347 mV for 20 hrs: Ni2P, Fe2p, and overall survey. The overall survey shows Ni, Fe, O, and C as the main components. The Ni2P peak demonstrates two characteristic signals of 2p_{1/2} and 2p_{3/2} in the range of 850-880 eV, while Fe2p peak shows two characteristic peaks in the range of 705-740 eV. All of these are similar to the ones before long-term electrolysis, indicating excellent stability of the electrode.

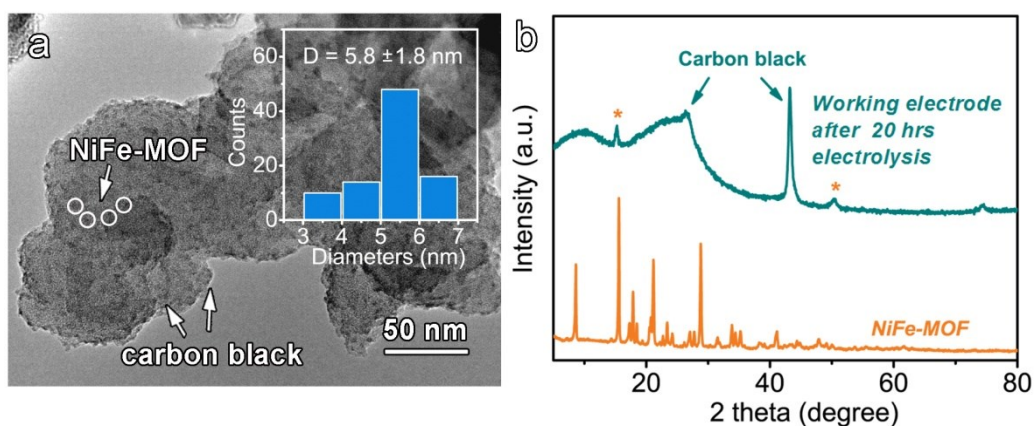


Figure S21: Structural characterizations of NiFe MOF-based working electrode after reaction at -347 mV for 20 hrs in nitrogen atmosphere: (a) HRTEM image and corresponding size distribution histograms; (b) XRD profiles.

Supporting note.

The morphology of the electrode was characterized by HRTEM (Figure S21a), which shows very small nanodots homogeneously embedded into carbon black matrix. Statistical analysis of the sizes of 50 nanodots is measured from HRTEM image, which shows NiFe-MOF has average particle size of 5.8 ± 1.8 nm. The particle size is comparable to its counterpart before N_2 electrolysis (5.5 ± 1.8 nm).

Further, the structure of NiFe-MOF-based electrode was determined by XRD (Figure S14b), which shows the dominant peaks of carbon black at around 27° and 42° . Of particular note, NiFe-MOF shows two characteristic peaks at around 15.6° and 48.0° , confirming the strong durability of working electrode toward electrochemical reactions.

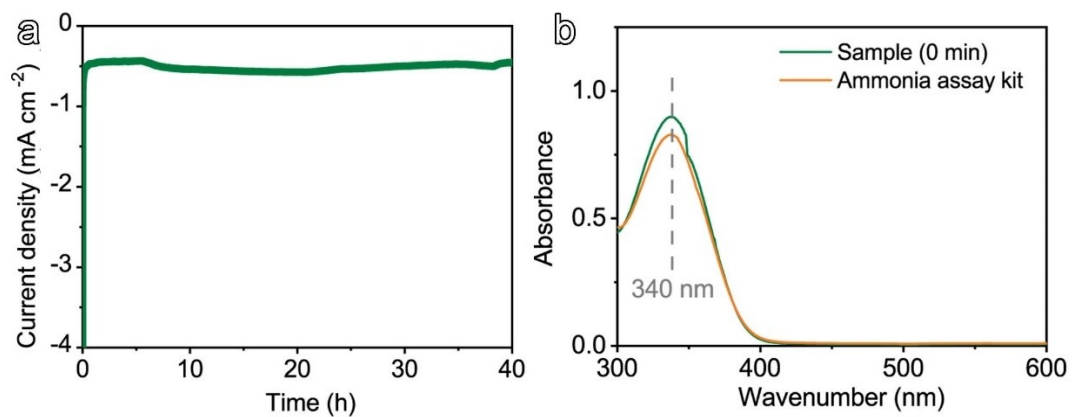


Figure S22: (a) Chronoamperometric response at -347 mV (vs. RHE) for 40 hrs. (b) UV-Vis curves of ammonia assay kit method with NiFe-MOF electrocatalyst after reaction at -347 mV (vs. RHE) for 40 hrs in nitrogen atmosphere

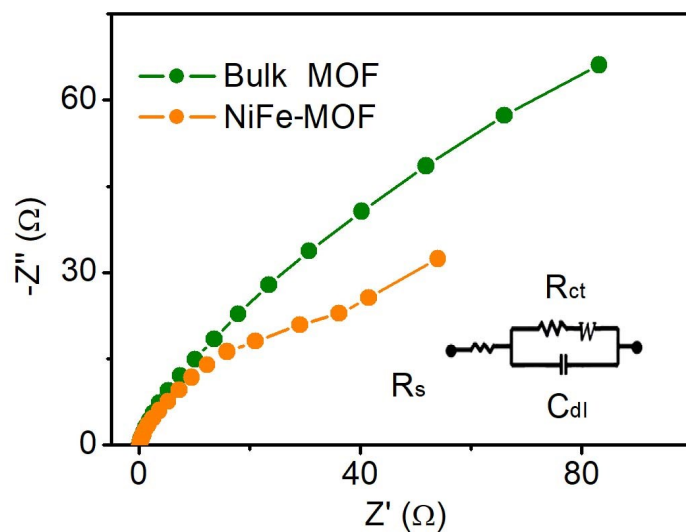


Figure S23: EIS spectrum of NiFe-MOF and bulk MOF. The charge transfer resistance (R_{ct}) has been estimated by the fitting the relevant curve to electrochemical circuit in the inset bottom right. The R_{ct} of NiFe-MOF is 22.3 ohm, which is much smaller than its bulk counterpart (58 ohm), thus indicating enhanced charge transport capability owing to downsizing effect.

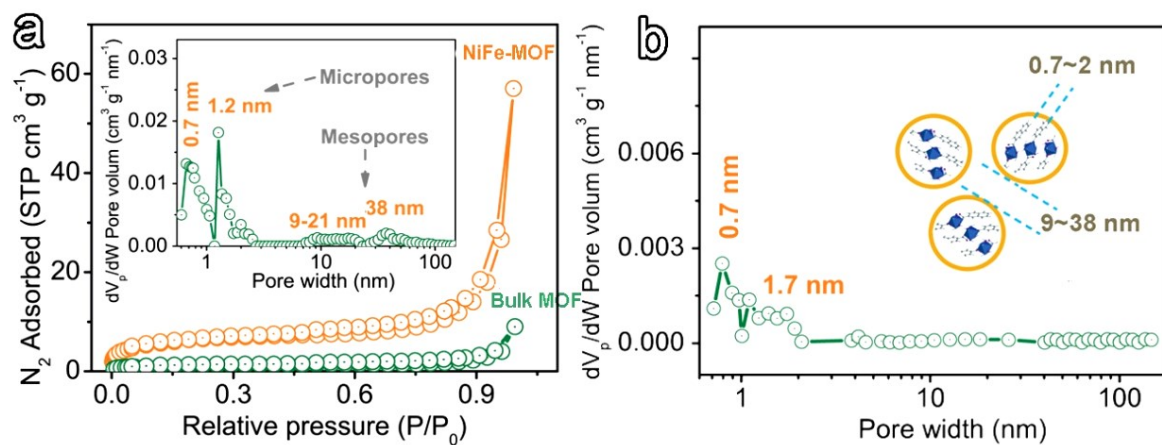


Figure S24: (a) Nitrogen adsorption-desorption isotherms (expressed in cm^3 STP g^{-1}) of NiFe-MOF in comparison with the bulk counterpart;^{12, 13} the inset of (a) shows corresponding pore size distribution of NiFe-MOF; (b) Size distribution of bulk MOF; the inset of (b) shows the schematic of micro- and mesopores inside NiFe-MOF.

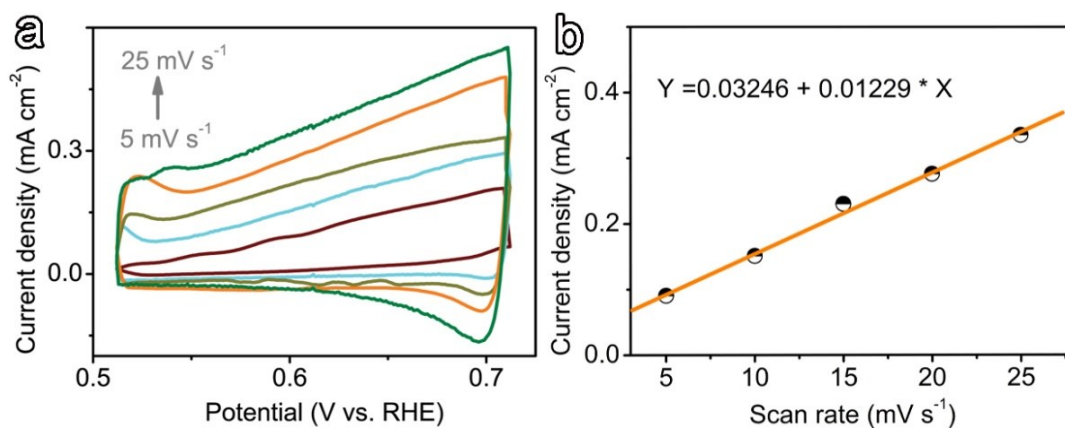


Figure S25: Roughness factor study of NiFe-MOF. The CVs (a) measured at different scan rates from 5 to 25 mV s⁻¹ in the potential region of 0.52-0.72 (vs. RHE); (b) the current density at 0.6 V (vs. RHE) is plotted against scan rate. The plot in panel (b) has a linear relationship and their slopes are the double layer capacitances (C_{dl}). Subsequently, the roughness factors (R_f) are calculated by dividing C_{dl} with $60 \mu\text{F cm}^{-2}$

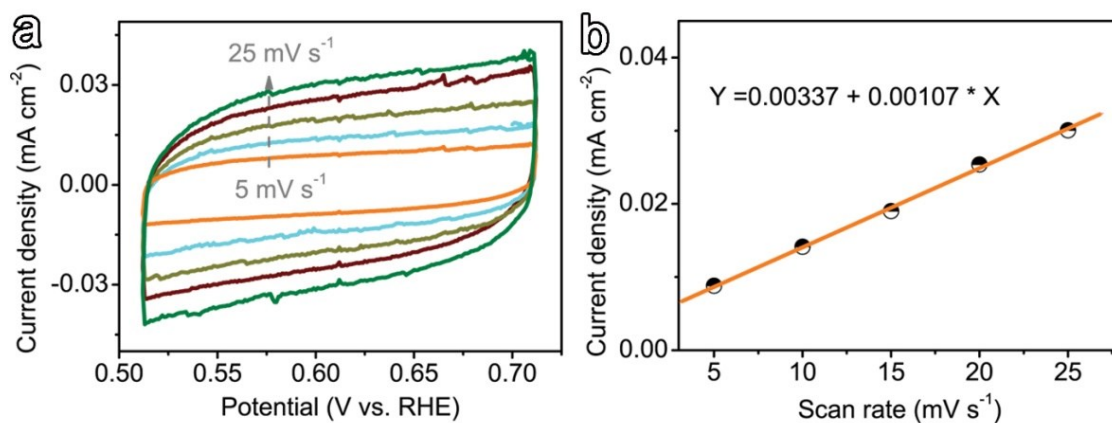


Figure S26: Roughness factor study of bulk MOF.¹⁴ The CVs (a) measured at different scan rates from 5 to 25 mV s⁻¹ in the potential region of 0.52-0.72 (vs. RHE); (b) the current density at 0.6 V (vs. RHE) is plotted against scan rate. The plot in panel (b) has a linear relationship and their slopes are the double layer capacitances (C_{dl}). Subsequently, the roughness factors (R_f) are calculated by dividing C_{dl} with 60 $\mu\text{F cm}^{-2}$.

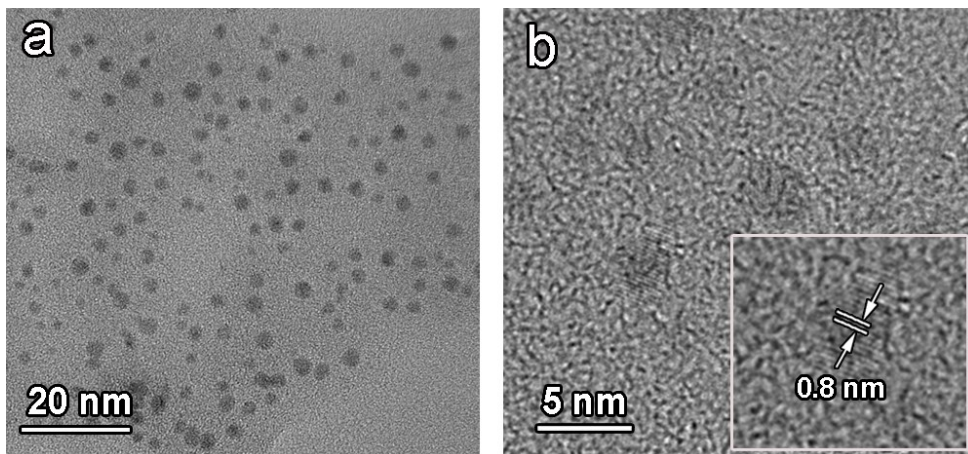


Figure S27: HRTEM images of 0D CuFe-MOF.

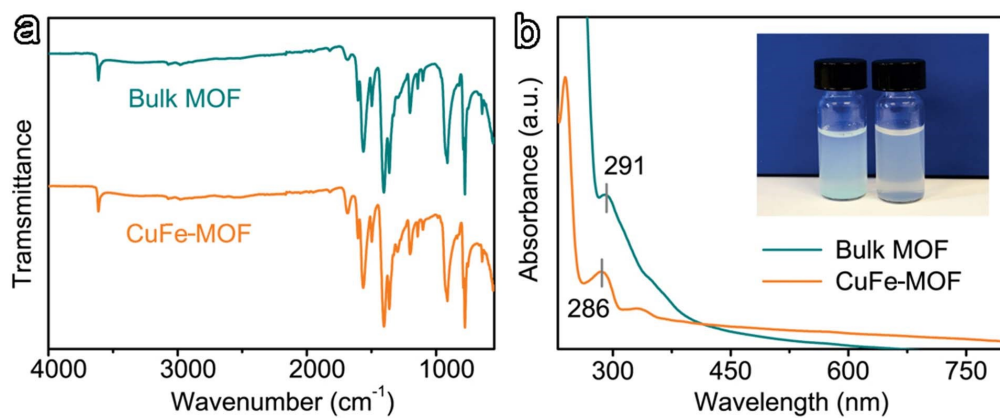


Figure S28: Structural characterizations of bulk and 0D CuFe-MOF: (a) FT-IR; (b) UV-vis; inset of (b) is the optical image showing the bulk MOF (left) and CuFe-MOF (right).

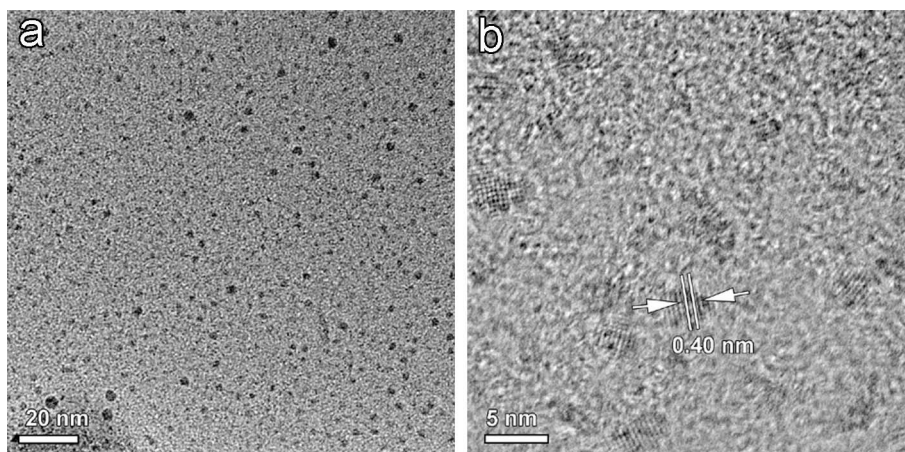


Figure S29: HRTEM images of 0D CoFe-MOF.

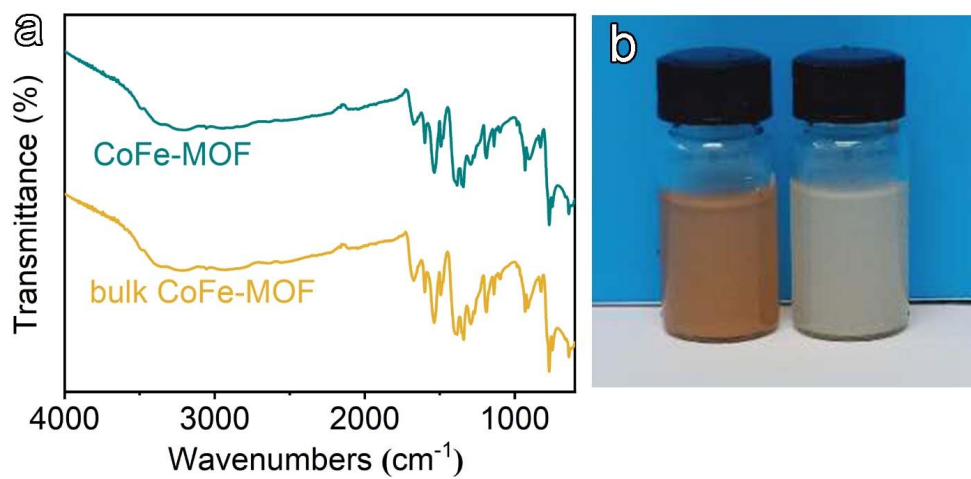


Figure S30: Structural characterizations of bulk and 0D CoFe-MOF: (a) FT-IR; (b) the optical image showing the bulk MOF (left) and 0D CoFe-MOF (right).

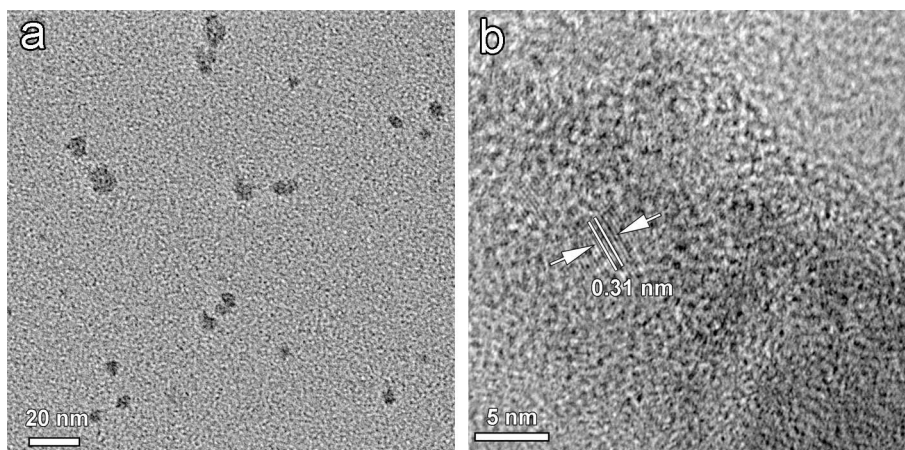


Figure S31: HRTEM images of 0D MnFe-MOF.

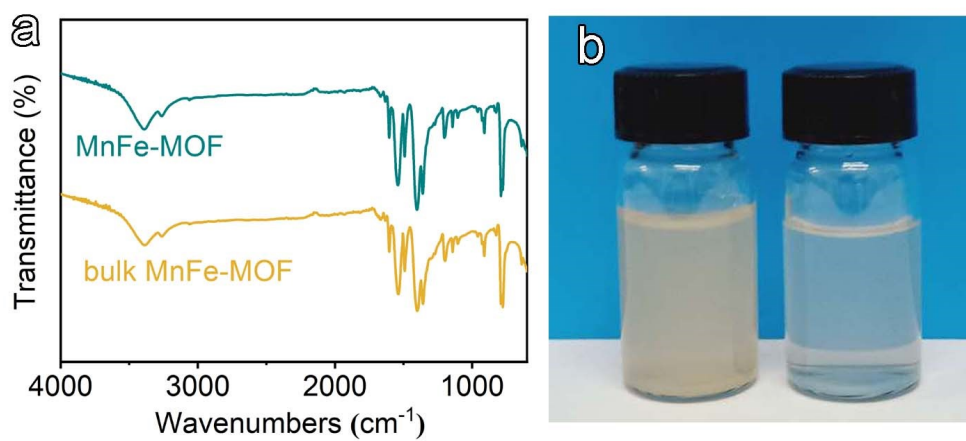


Figure S32: Structural characterizations of bulk and 0D MnFe-MOF: (a) FT-IR; (b) the optical image showing the bulk MnFe-MOF (left) and 0D MnFe-MOF (right).

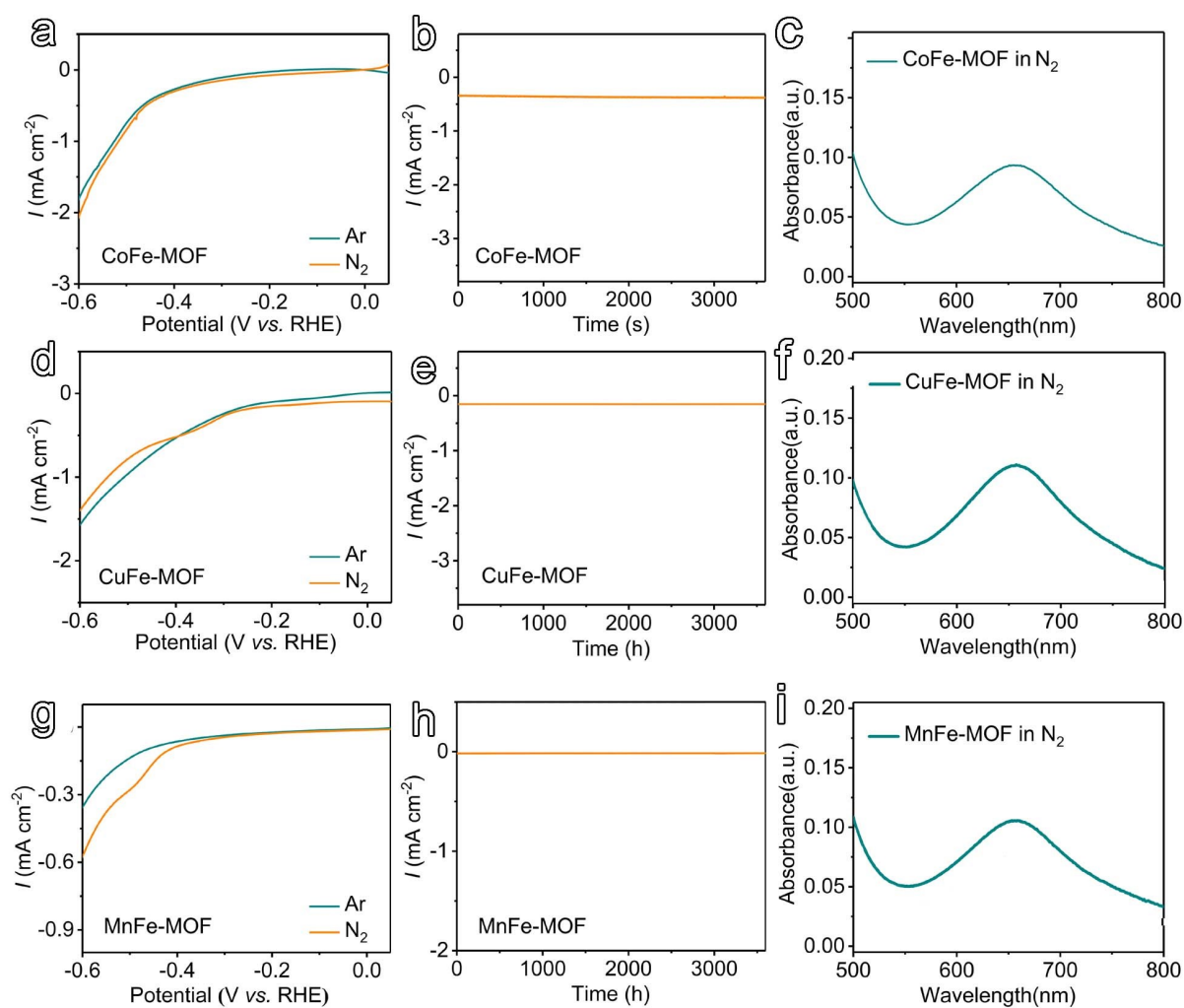


Figure S33: Electrocatalytic characterizations of CoFe-, CuFe-, and MnFe-MOFs for aqueous nitrogen reduction reaction (NRR) under ambient conditions. (a,d,g) The LSV plots in nitrogen and argon atmosphere. (b,e,h) Chronoamperometric response at -345 mV (vs. RHE). (c,f,i) UV-vis curves of indophenol blue assays for ammonia detection in nitrogen atmosphere.

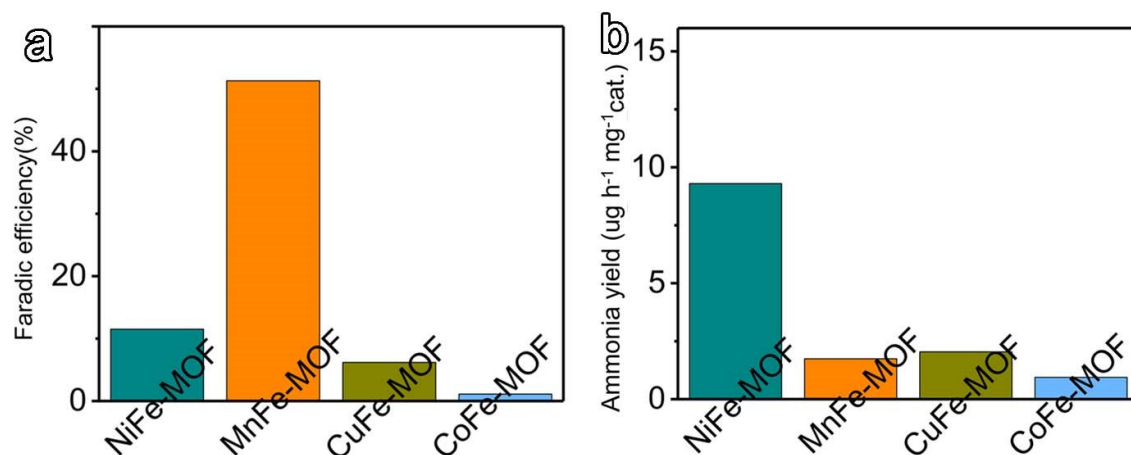


Figure S34: (a) Faraday efficiencies of different MOFs for aqueous nitrogen reduction reaction (NRR) under ambient conditions. (b) The corresponding ammonia production rates for NRR. It is shown that NiFe-, MnFe-, CuFe-, and CoFe-MOFs show the Faradic efficiencies of 11.5%, 51.3%, 6.2%, and 1.12%, and ammonia yield rates of 9.3, 1.74, 2.04, 0.94 $\mu\text{g h}^{-1} \text{mg}^{-1} \text{cat.}$, respectively. Therefore, MnFe-MOF shows the highest Faradic efficiency, while NiFe-MOF shows the highest ammonia yield rate for NRR.

Table S1. Comparison of the NRR activity for the synthesized NiFe-MOF with recently reported highly active electrocatalysts.

Catalyst	Faraday efficiency	Ammonia yield rate	Mass loading	Electrolyte	Supporting Reference
NiFe-MOF	11.5%	9.3 $\mu\text{g h}^{-1}$ $\text{mg}^{-1}_{\text{cat}}$	1 mg cm^{-2}	0.1 M NaHCO_3	This work
Au cluster/ TiO_2	8.11%	21.4 $\mu\text{g h}^{-1}$ $\text{mg}^{-1}_{\text{cat}}$	1 mg cm^{-2}	0.1 M HCl	1
Fe-(1,3,5-BTC) MOF	1.43%	2.12×10^{-9} $\text{mol s}^{-1} \text{cm}^{-2}$	8.3 mg cm^{-2}	2 M NaOH	15
$\text{Bi}_4\text{V}_2\text{O}_{11}/\text{CeO}_2$	10.16%	23.21 $\mu\text{g h}^{-1}$ $\text{mg}^{-1}_{\text{cat}}$	2 mg cm^{-2}	0.1 M HCl	2
MoS_2 /carbon fiber paper	1.17%	8.08×10^{-11} $\text{mol s}^{-1} \text{cm}^{-2}$	Not available	0.1 M Na_2SO_4	16
PdCu/graphene	2.8%	2.80 $\mu\text{g h}^{-1}$ $\text{mg}^{-1}_{\text{cat}}$	0.5 mg cm^{-2}	1 M KOH	17
Nitrogen-doped carbon film	5.2%	0.08 g m^{-2} h^{-1}	Not available	0.1 M HCl	18
PEBCD polymer	2.58%	2.01 $\mu\text{g cm}^{-2}$ h^{-1}	1.28 mg cm^{-2}	Li^+ -doped 0.5 MH_2SO_4	19
MoO_3	1.9%	29.43 $\mu\text{g h}^{-1}$ $\text{mg}^{-1}_{\text{cat}}$	1 mg cm^{-2}	0.1 M HCl	20
Fe/CNTs	0.15%	2.2×10^{-3} $\text{g m}^{-2} \text{h}^{-1}$	Not available	0.1 M KHCO_3	21
Au nanorods	4.0%	1.648 $\mu\text{g h}^{-1}$ cm^{-2}	1 mg cm^{-2}	0.1 M KOH	22
VN nanosheet array	2.25%	8.4×10^{-11} $\text{mol s}^{-1} \text{cm}^{-2}$	1.43 mg cm^{-2}	0.1 M HCl	23

N-doped porous carbon	1.5%	1.40 mmol g ⁻¹ h ⁻¹	1.6 mg cm ⁻²	0.05 M H ₂ SO ₄	24
trans-W(NNH ₂)TsO (Ph ₂ PCH ₂ CH ₂ PPh ₂) ₂ ⁺ complex	33%-36%	0.22-0.24 mol mol ⁻¹ _{cat}	Not available	Thf-0.2 M [NBu ₄][BF ₄]	25
tris(phosphine) borane iron(I)	23%-33%	3.4-4.6 mol mol ⁻¹ _{cat}	Not available	Anilinium triflate acids	26
Iron on nitrogen-doped carbon	56.55%	7.48 μg h ⁻¹ mg ⁻¹	1 mg cm ⁻²	0.1 M KOH	27
ZIF coated Ag-Au electrode	18±4%	10 pmol cm ⁻² s ⁻¹	-	LiCF ₃ SO ₃ /ethanol/THF electrolyte	28
Boron-rich covalent organic frameworks	45.43%	12.53 μg h ⁻¹ mg ⁻¹	1 mg cm ⁻²	0.1 M KOH	29

Table S2 Relative free energy changes for NiFe-MOF, Ni-MOF, and Fe-MOF during NRR process.

Reaction coordinate	Relative free energy changes for NiFe-MOF (eV)	Relative free energy changes for Ni-MOF (eV)	Relative free energy changes for Fe-MOF (eV)
* + N ₂	0	0	0
*N ₂	0.4	0.3	0.8
*N ₂ H	1.59	1.74	2.32
*NHNH	1.49	1.66	2.18
*NHNH ₂	1.67	1.53	1.87
*NH + NH ₃	1.44	2.41	2.22
*NH ₂	-0.07	0.37	0.37
*NH ₃	-0.97	-1.22	-0.69
* + NH ₃	-0.83	-0.83	-0.83

Supporting Note.

NRR reaction proceeds on the iron active sites of Fe-MOF *via* an associative distal pathway. As shown in Figure 4b and Table S2, nitrogen firstly binding on the Fe-MOF catalyst surface with a Gibbs free energy of 0.8 eV, which follows by a hydrogenation step (*N₂ + H⁺/e⁻ → *N₂H) with 2.32 V uphill after N₂ adsorption.

Next, the second and third proton-electron pair transfer takes place on the unhydrogenated nitrogen, leading to *NHNH and *NHNH₂ intermediates with the Gibbs free energy change to 2.18 eV and 1.87 eV. Consequently, the first NH₃ molecule can form after the fourth proton-electron pair transfer with another hydrogenation on the NH₂ moiety of *NHNH₂ with the free energy change to 2.22 eV. The relative Gibbs free energies for the fifth and sixth proton-electron pair transfer gains to produce *NH₂ and the final NH₃ species with the free energy of -0.37 and -0.69 eV, respectively. The catalytic reaction is closed by the release of second NH₃ molecule with an energy input of -0.83 eV.

As compared to NiFe-MOF, Fe-MOF shows significant higher Gibbs free energy for two rate-limiting steps, the first hydrogenation step (1.59 eV *vs.* 2.32 eV), and the first NH₃ molecule formation step (1.44 V *vs.* 2.22 eV). Therefore, DFT calculation indicates the introduction of Ni plays an important role for the first N₂ activation through hydrogenation and first NH₃ release processes during NRR.

Table S3. XANES NiL3 and FeL3 peak intensity ratios of Bulk MOF and NiFe-MOF with respect to Ni and Fe foils (Figures 4c,d).

XANES L edge peak	Peak position	Peak intensity ratio of bulk MOF vs. metal foils	Peak intensity ratio of NiFe-MOF vs. metal foils
Ni L3	852 eV	1.2	0.89
Ni L3	855 eV	1.46	1.25
Fe L3	778 eV	0.35	0.3
Fe L3	780 eV	0.57	0.41

Supporting Note.

It shows that XANES profile of NiFe-MOF is characteristic of a number of peaks, for example, nickel L3 edge peaks located at 852 eV. This peak indicates tetrahedrally coordinated Ni²⁺ inside NiFe-MOF structure. Note that the peak intensity ratio with respect to that of nickel foils can reveal the amounts of Ni²⁺, which is 0.89 for Ni L3 at 852 eV. In great contrast, this value inside bulk MOF is 1.2. Therefore, the amount of Ni²⁺ increased in NiFe-MOF as comparison to its bulk counterpart, thus indicating a decrease of oxidation state as a result of the downsizing effect.

Supplementary Reference

1. M. M. Shi, D. Bao, B. R. Wulan, Y. H. Li, Y. F. Zhang, J. M. Yan and Q. Jiang, *Adv. Mater.*, 2017, **29**, 1606550.
2. C. D. Lv, C. S. Yan, G. Chen, Y. Ding, J. X. Sun, Y. S. Zhou and G. H. Yu, *Angew. Chem. Int. Ed.*, 2018, **57**, 6073-6076.
3. J. P. Perdew, K. Burke and M. Ernzerhof, *Phys. Rev. Lett.*, 1996, **77**, 3865-3868.
4. G. Kresse and D. Joubert, *Phys. Rev. B*, 1999, **59**, 1758-1775.
5. G. Kresse and J. Furthmüller, *Comput. Mater. Sci.*, 1996, **6**, 15-50.
6. G. Kresse and J. Furthmüller, *Phys. Rev. B*, 1996, **54**, 11169-11186.
7. S. Grimme, S. Ehrlich and L. Goerigk, *J. Comput. Chem.*, 2011, **32**, 1456-1465.
8. G. Chen, Y. Zhu, H. M. Chen, Z. Hu, S. F. Hung, N. Ma, J. Dai, H. J. Lin, C. T. Chen, W. Zhou and Z. Shao, *Adv. Mater.*, 2019, **31**, e1900883.
9. J. Zhang, J. Liu, L. Xi, Y. Yu, N. Chen, S. Sun, W. Wang, K. M. Lange and B. Zhang, *J. Am. Chem. Soc.*, 2018, **140**, 3876-3879.
10. Y. Hou, H. Kondoh, T. Ohta and S. Gao, *Appl. Surf. Sci.*, 2005, **241**, 218-222.
11. M. Zeng and Y. Li, *J. Mater. Chem. A*, 2015, **3**, 14942-14962.
12. M. Kruk, M. Jaroniec and A. Sayari, *Langmuir*, 1997, **13**, 6267-6273.
13. T. Tillotson and L. Hrubesh, *J. Non-Cryst. Solids*, 1992, **145**, 44-50.
14. Y. Li, P. Hasin and Y. Wu, *Adv. Mater.*, 2010, **22**, 1926-1929.
15. X. Zhao, F. Yin, N. Liu, G. Li, T. Fan and B. Chen, *J. Mater. Sci.*, 2017, **52**, 10175-10185.
16. L. Zhang, X. Ji, X. Ren, Y. Ma, X. Shi, Z. Tian, A. M. Asiri, L. Chen, B. Tang and X. Sun, *Adv. Mater.*, 2018, **30**, e1800191.
17. M.-M. Shi, D. Bao, S.-J. Li, B.-R. Wulan, J.-M. Yan and Q. Jiang, *Adv. Energy Mater.*, 2018, **8**, 1800124.
18. H. Wang, L. Wang, Q. Wang, S. Ye, W. Sun, Y. Shao, Z. Jiang, Q. Qiao, Y. Zhu, P. Song, D. Li, L. He, X. Zhang, J. Yuan, T. Wu and G. A. Ozin, *Angew. Chem. Int. Ed.*, 2018, **57**,

12360-12364.

19. G.-F. Chen, X. Cao, S. Wu, X. Zeng, L.-X. Ding, M. Zhu and H. Wang, *J. Am. Chem. Soc.*, 2017, **139**, 9771-9774.
20. J. Han, X. Ji, X. Ren, G. Cui, L. Li, F. Xie, H. Wang, B. Li and X. Sun, *J. Mater. Chem. A*, 2018, **6**, 12974-12977.
21. S. Chen, S. Perathoner, C. Ampelli, C. Mebrahtu, D. Su and G. Centi, *Angew. Chem. Int. Ed.*, 2017, **56**, 2699-2703.
22. D. Bao, Q. Zhang, F.-L. Meng, H.-X. Zhong, M.-M. Shi, Y. Zhang, J.-M. Yan, Q. Jiang and X.-B. Zhang, *Adv. Mater.*, 2017, **29**, 1604799.
23. R. Zhang, Y. Zhang, X. Ren, G. Cui, A. M. Asiri, B. Zheng and X. Sun, *ACS Sustain. Chem. Eng.*, 2018, **6**, 9545-9549.
24. Y. Liu, Y. Su, X. Quan, X. Fan, S. Chen, H. Yu, H. Zhao, Y. Zhang and J. Zhao, *ACS Catal.*, 2018, **8**, 1186-1191.
25. C. J. Pickett and J. Talarmin, *Nature*, 1985, **317**, 652-653.
26. M. J. Chalkley, T. J. Del Castillo, B. D. Matson and J. C. Peters, *J. Am. Chem. Soc.*, 2018, **140**, 6122-6129.
27. M. Wang, S. Liu, T. Qian, J. Liu, J. Zhou, H. Ji, J. Xiong, J. Zhong and C. Yan, *Nat. Commun.*, 2019, **10**, 341.
28. H. K. Lee, C. S. L. Koh, Y. H. Lee, C. Liu, I. Y. Phang, X. Han, C. K. Tsung and X. Y. Ling, *Sci. Adv.*, 2018, **4**, eaar3208.
29. S. Liu, M. Wang, T. Qian, H. Ji, J. Liu and C. Yan, *Nat. Commun.*, 2019, **10**, 3898.